J Mater Sci (2010) 45:6528–6539
DOI 10.1007/s10853-010-4742-7

Temperature and stress fields evolution during spark plasma sintering processes

S. Muñoz · U. Anselmi-Tamburini

Received: 5 February 2010 / Accepted: 25 June 2010 / Published online: 13 July 2010

Abstract Numerical modelling of Spark Plasma Sintering (SPS) processes is essential to evaluate temperature and stress distributions that can result in sample inhomogeneities. Most of the available literature, however, produced analysis in static conditions. In this work, we focused our attention on the time evolution of current density, temperature and stress distribution during a SPS process using a new approach that includes a PID control in the algorithm, allowing a realistic simulation of experiments performed using a temperature controller. Controlled temperature experiments have been simulated and discussed, with special interest focused on the time evolution of the process. The results showed that stress gradients inside the samples ($\sim$40%) are much greater than the temperature gradients ($\sim$2%), suggesting that heterogeneities in the microstructure can also be caused by the stress gradient. During the evolution of the process, a peak in stresses is experienced by the alumina sample at the beginning of the cooling stage, caused by differences in contraction between the sample and the die. It has been proved that, using a controlled cooling stage, these peaks in the stresses can be easily eliminated.

S. Muñoz (✉)
Department of Mechanical and Materials Engineering, Escuela Superior de Ingenieros, Universidad de Sevilla, Camino de los Descubrimientos s/n, 41092 Sevilla, Spain
e-mail: sergiomunoz@us.es

S. Muñoz · U. Anselmi-Tamburini
Department of Physical Chemistry, University of Pavia, Viale Taramelli 16, 27100 Pavia, Italy

Introduction

Spark plasma sintering (SPS) is a powder consolidation technique that employs pulsed electric current and mechanical pressure to assist the sintering [1, 2]. When compared with more traditional approaches, SPS shows important advantages, such as a short processing time, the elimination of sintering aids and high heating rates that minimise the grain growth, all of which lead to materials with improved properties [3]. Despite all of its advantages, SPS is characterized by relevant temperature and stress inhomogeneities that might eventually produce inhomogeneities in the sample microstructure, particularly in the case of large samples or near net-shaped parts [3, 4]. For this reason, a precise understanding of the current, temperature and stress distributions and of their time evolution is essential for the development of the SPS process. Numerical modelling is particularly relevant in this respect, due to the difficulties involved in an experimental investigation of these parameters. Recently, there have been several works that used the finite element method to investigate the current and temperature distributions in the SPS [5–11]. These studies, however, present some quite dissimilar characteristics. Only some of them, for instance, took into account the presence of contact resistances [5, 6, 8, 9], while the mechanical aspects, such as the analysis of stress distributions, have been generally neglected. This is a critical omission, because experimental studies have demonstrated that processing pressure is of crucial importance in densification mechanisms [3, 4]. The only exceptions are represented by the work by Wang et al. [11] and Antou et al. [10], which developed a coupled electrical–thermal–mechanical analysis. In the study by Wang et al., the electrical and mechanical problems have been treated as quasistatic, although their approach is in principle

capable to produce time-dependent analysis. This choice, however, did not allow to appreciate some of the complexities derived from the solution of the three coupled, non-linear, full transient fields. In most of the literature on SPS modelling the current is maintained constant throughout the simulation. Although this produces results that are more realistic of the one obtained from the steady-state solutions, they still represent a situation quite different from the common experimental conditions. In actual SPS experiments, in fact, the current is never constant, but is changed in order to follow a pre-defined temperature cycle. Aim of this paper is actually to clarify the peculiarities related with this complex current profiles used in typical SPS experiments. In the work by Antou et al. [10] time dependence has been included, making use of experimental data of electric current absorbed by a real apparatus during a specific experiment, an approach that lacks generality and cannot be applied when a simulation corresponding to a different set of experimental parameters is considered. McWilliams and Zavaliangos [8] modelled the temperature evolution imposing a linear current increase, producing time evolution of the temperature that deviate considerably from the linear trend generally followed in temperature-controlled experiments. In another work of these authors [9], although the mechanical strain is not explicitly considered, a model for the powder densification is introduced. In the present work we introduce a finite element model that uses a three-way coupled full transient analysis that is able to simulate the thermal, electrical and mechanical time-dependent behaviours of the SPS process, but is also able to reproduce temperature-controlled experiments, as they are typically performed in SPS apparatuses. Since no direct solution of the temperature-controlled problem is possible, as it represents a typical inverse problem, in this work, we propose an approach that includes a proportional–integral–derivative control (PID) algorithm in the model, allowing a realistic simulation of typical SPS experiments in which a preset time–temperature profile is imposed. The model includes also electrical and thermal contact resistances, since these terms play a crucial role in defining the temperature distribution in the SPS assembly. Our model, on the other hand, does not include any description of the sample densification, as we are more interested to understand the nature of the forces acting on the sample, that to produce a faithful reproduction of the experimental results. The finite element model proposed in this work provides a framework that can be used to study the influence of different parameters (specimen and die material, dimensions of the set-up, control parameters, etc.) on the temperature and stress distributions inside the sample, and it can help to optimise the production processes of large and near net-shaped parts with controlled properties.

Experimental procedure

The SPS sintering machine used in this study is shown schematically in Fig. 1a, corresponding to the setup of an SPS SYNTEX 2050 apparatus. It is based on a graphite die containing the sample, two plungers that are in direct contact with the specimen, six different spacers and two electrodes on the top and bottom of the set-up. The die, plungers and spacers are made of conductive graphite,

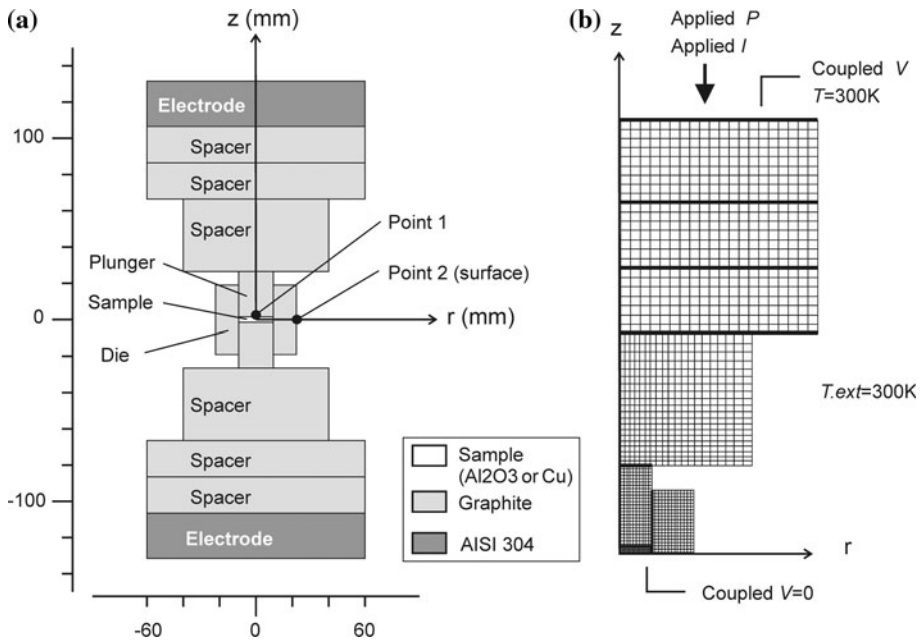

Fig. 1 **a** Schematic cross-section of the spark plasma sintering apparatus, showing dimensions in mm. **b** Finite element mesh, with boundary conditions and loads used for the simulation defined

whereas the electrodes are made of stainless steel. Two different sample materials with widely differing properties have been used in this work: (a) fully dense alumina and (b) fully dense copper. All dimensions of the set-up are specified in Fig. 1a. The specimen dimensions are 19 mm diameter and 3 mm thickness. The plungers are 19 mm in diameter and 25 mm long. The die has an external diameter of 44.5 mm and is 38 mm tall.

The whole set-up is placed in a vacuum chamber whose walls are held at room temperature (300 K). The two extreme upper and lower surfaces of the electrodes are maintained at a constant temperature of 300 K through a water cooling system. Experimental evaluation of the temperature was made using two different methods: a K-type bare thermocouple positioned in a hole drilled along the axis of the upper plunger and ending 0.5 mm above the upper surface of the sample (point 1 in Fig. 1a), and an optical pyrometer reading temperature of the external surface of the graphite die (point 2 in Fig. 1a).

In real experiments, the mechanical load is applied to the top electrode. The electrical power is supplied by applying a voltage difference between the electrodes, and in this manner a current intensity flows through the entire assembly, from the top to the bottom electrode. There are two different SPS operational modes: current control and temperature control. In the current intensity control, power is controlled through the application of a variable voltage difference between the electrodes in order to produce a preset time–current profile, $I(t)$. In the temperature control, power is controlled by a determinate temperature measurement, i.e., a closed-loop control system controlling the variable voltage difference applied between the electrodes (and, in this way, the current flowing through the set-up), in such a way that a preset time–temperature profile is followed, $T(t)$.

Finite element model

The finite element model is based on a set of governing equations that involve a three-way coupling of the electrical, thermal and mechanical problems. Since the material properties are temperature dependent and there is a direct influence among the three problems, iterations among the three physics fields are needed for convergence. The numerical solution of the electrical–thermal–mechanical coupled problem has been obtained using a three-way coupled full transient analysis, developed in the commercial finite element code ANSYS. The procedure for the coupled-field analysis has been the direct coupled-field method [12]. Because of the temperature dependence of the material properties, these are updated at each node at every time step.

Figure 1a presents the cross-section of the SPS set-up used for the simulation. Taking advantage of the axisymmetrical configuration, only the two-dimensional section shown in Fig. 1b in cylindrical coordinates is studied. A two-dimensional numerical simulation has been run using a mesh (Fig. 1b) of quadrilateral high order coupled-field elements (eight nodes and four degrees of freedom per node: displacement in r and z directions, temperature and electric potential) with the axisymmetric option. Horizontal and vertical contacts among the different constituent parts of the set-up, represented as a thick line in Fig. 1b, have also been modelled for the three coupled problems (electrical, thermal and mechanical).

Regarding the mechanical problem, the graphite used in the SPS experiments is dense and polycrystalline, and thus it is treated as isotropic in the model. Although a real SPS experiment always uses powder as a sample, in our model the specimen is modelled as an isotropic dense solid, simplifying the model and not addressing the complicated densification process. Because of this simplification, the simulations represent a good approximation of the problem in the latter stages of the densification process (final stage of sintering). It should be noted that this simplification has also been used in all previous studies [5–11]. Although a relatively complex current pulse pattern is generally used in commercial SPS apparatuses, DC current has been used in the finite element model. As demonstrated by others [7], this is a good approximation since most of the energy in the process is delivered at low frequencies with a very large portion at 0 Hz, corresponding to DC current. This also implies that current fluxes in the die are not expected to present any skin effects, as could be expected in a high frequency conduction problem [7]. All the electrical, thermal and mechanical material properties used in the numerical modelling are listed as temperature-dependent functions in the Appendix.

Basic relationships

The electrical potential distribution is governed by the following partial differential equation:

$$\nabla \cdot \boldsymbol{J} = 0, \tag{1}$$

where $\boldsymbol{J} = \sigma \boldsymbol{E}$ is the current density, $\boldsymbol{E}$ is the electric field and σ is the electrical conductivity. Considering that $\boldsymbol{E} = -\nabla V$, with V being the electric potential, Eq. 1 can be written as

$$\nabla \cdot \boldsymbol{J} = \nabla \cdot (\sigma \boldsymbol{E}) = \nabla \cdot (-\sigma \nabla V) = 0. \tag{2}$$

The temperature distribution is based on the partial differential heat equation:

$$\rho c_p \frac{\partial T}{\partial t} = \nabla \cdot (k \nabla T) + \dot{q}_J + \dot{q}_c + \dot{q}_{conv} + \dot{q}_{rad} + \dot{q}_{ec}, \quad (3)$$

where ρ is the density, c_p the heat capacity, T the temperature and k the thermal conductivity. The term $\dot{q}_J = \boldsymbol{J} \cdot \boldsymbol{E} = J \cdot E$ represents the heat generated by Joule heating per unit volume per unit time. The last four terms of the Eq. 3, $\dot{q}_c$, $\dot{q}_{conv}$, $\dot{q}_{rad}$ and $\dot{q}_{ec}$, are surface heat fluxes that correspond to heat conduction from neighbouring volumes, heat transfer by convection, heat transfer by radiation and interfacial heating effects. In our problem, because the experiments are performed in vacuum, the heat transfer by convection, $\dot{q}_{conv}$, is zero. The heat transfer by radiation, $\dot{q}_{rad}$, is given by:

$$\dot{q}_{rad} = \sigma_S \varepsilon \left[T_1^4 - T_2^4\right], \quad (4)$$

where $\sigma_S = 5.669 \times 10^{-8}$ W m^{-2} K^{-4} is the Stefan–Boltzmann constant, ε is the emissivity and T_1 and T_2 are the temperatures of the emitting and absorbing surfaces, respectively. A value of $\varepsilon = 0.8$ for graphite has been taken, which has been proven to be very realistic [5, 6]. Heat transfer by radiation among the exposed surfaces of the die, plungers, spacers, electrodes and interior chamber surface has been taken into account using a geometric viewing factors algorithm that is readily available in commercial finite element codes (e.g. ANSYS or ABAQUS).

In order to solve the mechanical problem, the mechanical displacement field must be calculated. Because no yield stress is reached for any material in our problem, a linear elastic calculation has been done. In case the yield stress is reached, a more complicated non-linear elasto-plastic calculus is needed. The set of governing equations for a linear elastic problem is compounded for equilibrium and constitutive equations as well as the strain–displacements relationship equation, all in vector notation:

$$\nabla \cdot \boldsymbol{\sigma} + \boldsymbol{F} = 0, \quad (5)$$

$$\boldsymbol{\varepsilon} = \frac{1}{2\mu}[\boldsymbol{\sigma} - \nu(\mathrm{tr}\boldsymbol{\varepsilon})\boldsymbol{I}] + \alpha_T \Delta T \boldsymbol{I} \quad (6)$$

and

$$\boldsymbol{\varepsilon} = \frac{1}{2}\left[\nabla \boldsymbol{u} + (\nabla \boldsymbol{u})^T\right], \quad (7)$$

where $\boldsymbol{\sigma}$ is the stress tensor, $\boldsymbol{F}$ the body force per unit volume, $\boldsymbol{\varepsilon}$ the strain tensor and $\boldsymbol{u}$ the displacement vector. α_T is the thermal expansion coefficient and $\mu = E/2(1 + \nu)$ is the Lamé coefficient, where E is the Young's modulus and ν is the Poisson's ratio. In calculating the mechanical displacement field, friction is neglected at the contact interfaces.

Contact resistances

In order to correctly model the contact among the different parts of the set-up, thermal and electrical contact resistances must be taken into account [5, 6]. It has been experimentally demonstrated that thermal and electrical resistances induced at the contacts between the different constituent parts of the set-up have a large influence on the temperature and electrical potential fields [6]. It must be noted that the values of both thermal and electrical contact resistances depend on the applied pressure: increasing the mechanical pressure, the influence of contact resistances becomes less important. However, it has been demonstrated by Vanmeensel et al. [6], that the contact resistance, especially on vertical contacts, must always be included in any reliable modelling of SPS, since they play a very important role in defining the temperature and current distribution. The thermal and electric fluxes between two contacting surfaces are defined by [13]:

$$\dot{q}_{contact} = h_g \Delta T \quad (8)$$

and

$$J_{contact} = \sigma_g \Delta V, \quad (9)$$

where h_g and σ_g are the thermal and electrical contact conductance coefficients, respectively, and ΔT and ΔV are the temperature and potential differences between the two surfaces in contact. In addition to the drop of temperature and voltage, the heat flux is also discontinuous at the interface as Joule heat is generated due to the electric contact resistance:

$$\dot{q}_{ec} = J_{contact} \Delta V = \sigma_g (\Delta V)^2. \quad (10)$$

It is interesting to note that if there is no electric current and only heat flows across the imperfect interface, then the heat flux will be continuous since no thermal energy is generated or absorbed there.

Initial and boundary conditions, and applied loads

The initial and boundary conditions used for the analysis are the following (Fig. 1b): (a) the initial temperature in the whole set-up is 300 K; (b) the experiments take place in vacuum, so heat losses by convection are neglected; (c) the temperature of the chamber surface is set constant as 300 K during the entire process; (d) the temperature of the top surface of the electrode is set constant as 300 K due to the refrigeration and (e) the electric potential in nodes of the top surface of the electrode is coupled (with a value V), as well as in nodes at $z = 0$ (with a value $V = 0$). Thus, there is an electric potential difference $\Delta V = V$ through the extremes of the studied section. Figure 1b shows the applied loads; a mechanical distributed pressure, P, and an electrical current intensity, I, are directly applied on the top surface of the electrode.

PID control

As mentioned earlier, there are two different ways to control the electrical power in an SPS apparatus: current intensity control and temperature control. In the current intensity control, a preset time–current profile, $I(t)$, is directly applied to the top surface of the electrode. In the temperature control, the applied electrical power is controlled by a temperature measurement, i.e. a closed-loop control system controlling the current intensity, $I(t)$, in such a way that a preset time–temperature profile is followed, $T(t)$. For the simulation of an experiment with temperature control, a proportional–integral–derivative control (PID) has been programmed [14] and integrated into the ANSYS code. A PID controller attempts to correct the error between a measured process variable (in our case, a temperature) and a desired set-point by calculating and then outputting a corrective action, which can adjust the process accordingly and rapidly in order to keep the error minimal. The PID controller works in a closed-loop configuration (Fig. 2). The variable $e(t)$ represents the tracking error, i.e. the difference between the desired temperature, $T(t)$, and the actual temperature, $T_{act}(t)$, of the control point. This error signal $e(t)$ is sent to the PID controller, and the controller computes both the derivative and the integral of this error signal. The value of the current intensity, $I(t)$, is given by the equation:

$$I(t) = K_P \cdot e(t) + K_I \cdot \int_0^t e(\tau)d\tau + K_D \frac{de(t)}{dt}, \qquad (11)$$

where K_P, K_I and K_D are the proportional, integral and derivative gains, respectively.

Once the PID control has been programmed, a set of PID controller parameters (K_P, K_I and K_D gains) must be chosen for an optimum control response. For the adjustment of the PID control parameters, the Ziegler–Nichols method [15] has been used. It is noteworthy that if there is any change in the SPS system (materials, dimensions, etc.), the PID control parameters must be readjusted.

Finite element model verification

To demonstrate the accuracy of the finite element model presented in this work, several different experiments have been simulated and compared with actual experiments. These experiments have been performed using an SPS SYNTEX 2050 apparatus. The duration of the experiments was 900 s. A constant mechanical load of 11.5 KN was applied to the top electrode and maintained during the entire experiment, corresponding to a pressure on the top electrode of $P = 1.0168$ MPa and a nominal applied pressure on the sample of 40.56 MPa. Experiments have been carried out while maintaining the current constant at $I = 1000$ A for 600 s. The electrical power is then turned off, and the current $I = 0$ A is kept from 600 to 900 s. Two sample materials with very different thermal, electrical and mechanical properties have been used in the experiments: (a) fully dense alumina and (b) fully dense copper. As mentioned early, thermal and electrical contact resistances have been included in the model. Zavaliangos et al. and Vanmeensel et al. [5, 6] calibrated the thermal and electrical contact resistances based on a series of experiments without specimens. Both works showed that vertical contacts exhibit higher thermal and electrical resistances than horizontal ones. It has been assumed that both the thermal and electrical contact conductance coefficients of the vertical contacts, $h_{g)V}$ and $\sigma_{g)V}$, are proportional to the coefficients of the horizontal contacts, $h_{g)H}$ and $\sigma_{g)H}$ [6]. The best correlation between the experimental and calculated results in the simulations of this work has been obtained with the following coefficients values:

- $h_{g)H} = 15 \times 10^3$ W m^{-2} K^{-1} and $\sigma_{g)H} = 5 \times 10^7$ Ω^{-1} m^{-2}, for horizontal contacts, and
- $h_{g)V} = h_{g)H}/6$ and $\sigma_{g)V} = \sigma_{g)H}/6$, for vertical contacts.

These values of the thermal and electrical contact conductance coefficients are on the same order as those used by other authors [5, 6].

In Fig. 3, the simulated temperature evolution at points 1 and 2 (Fig. 1a) during the process are compared with the experimental results, for both the alumina and copper samples. As is shown, the simulated and experimental results are in reasonable agreement. From the experimental results in Fig. 3, several aspects observed by other authors [5–11] are confirmed. One such aspect is that higher temperatures are reached in the non-conducting sample (alumina) than in the conducting one (copper), with important differences in temperature between the sample (point 1) and the die surface (point 2). These differences in temperature between the sample and the external surface suggest an important radial temperature gradient in the sample and in the die, as has been reported in several experimental works [16, 17], that can produce heterogeneities in the chemical composition and microstructure of the sample.

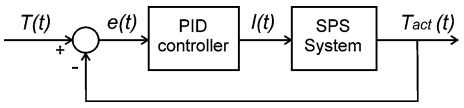

Fig. 2 Schematic of the PID controller

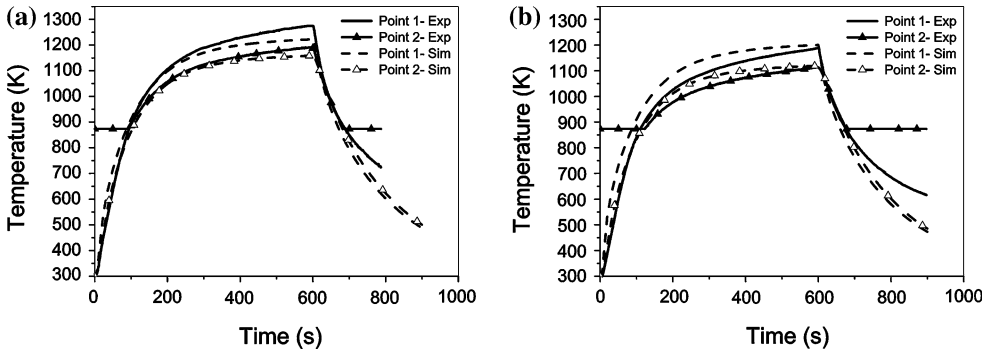

Fig. 3 Experimental and simulated temperature evolution at points 1 and 2 (defined in Fig. 1a), for **a** alumina and **b** Cu samples

Results and discussion

Once the accuracy of the proposed model was proven, a detailed study of the evolution of the three coupled fields (electrical, thermal and mechanical) in the SPS process was performed. Because real SPS experiments are usually carried out using temperature control, all simulations used in this study have been performed using this kind of control. In order to study the influence of sample material on the SPS process, two different sample materials have been simulated: (a) fully dense alumina and (b) fully dense copper. Figure 4 shows a three-dimensional representation of the sample, as well as the ABCD section, studied in the finite element model of Fig. 1b. From now on, all results will refer only to the ABCD section.

Simulated experiments have been carried out by controlling the temperature of the centre of the sample (point A in Fig. 4) and following a pre-determined time–temperature profile, $T(t)$, that involves a linear increase from 300 to 1300 K in 300 s (200 K/min). From 300 to 600 s, a constant value of 1300 K is maintained and, finally, at 600 s the electrical power is turned off. The total duration of the simulated experiments is 900 s. Figure 5a shows the target time–temperature profile $T(t)$ (dashed line) and the actual simulated temperature of point A (solid line) for the alumina sample. In the detail of the zone near 1300 K shown in Fig. 5a, the typical behaviour of a PID-controlled

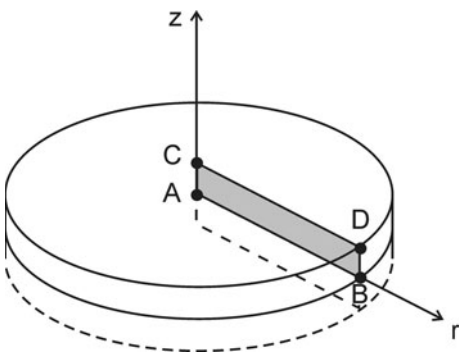

Fig. 4 Representation of the sample, with the ABCD section used in the model

variable can be seen, in which, after some small oscillations, a stable value is reached. Figure 5b shows the applied current intensity, $I(t)$, calculated by the PID control in order to obtain the time–temperature profile, $T(t)$, of Fig. 5a. As shown, after a non-linear increase in the current during the heating ramp, a drop of the current intensity is observed at time $t = 300$ s in order to stabilise the controlled temperature to 1300 K. From 300 to 600 s, a slight decrease of the current intensity is observed in order to compensate for the gradual heating of the large ram cylinders. The PID control parameters have been adjusted for both cases at $K_P = 7.5$, $K_I = 0.1$ and $K_D = 40$ for alumina and $K_P = 7$, $K_I = 0.12$ and $K_D = 10$ for copper.

Temperature distribution

Temperature distribution in the SPS die-sample assembly under static conditions has been analyzed thoroughly in several previous publications [5–11]. Because heating in the SPS process is resistive, the temperature distribution is directly dependent on the current distribution in the set-up. As a result, in the case of alumina, higher temperatures are reached in the die, while the temperatures in the punch close to the sample surface are lower. The difference in temperature distribution in the two cases can be better appreciated when only the sample is considered (Fig. 6). Inside the alumina sample, a temperature gradient is observed in both radial and axial directions, with larger differences in temperature in the radial direction (22 K between points A and B) than in the axial one (7 K between points D and B). However, in the copper sample, a very homogeneous temperature distribution is observed, with a difference of only 4 K in the radial direction (between points A and B) and no difference in the axial one. The temperature distribution inside the sample is governed mainly by its thermal conductivity: the lower thermal conductivity of alumina leads to a non-homogeneous temperature distribution with significant gradients, while the higher thermal conductivity of copper leads to a homogeneous temperature inside the sample. In conclusion, due to the importance of temperature in the

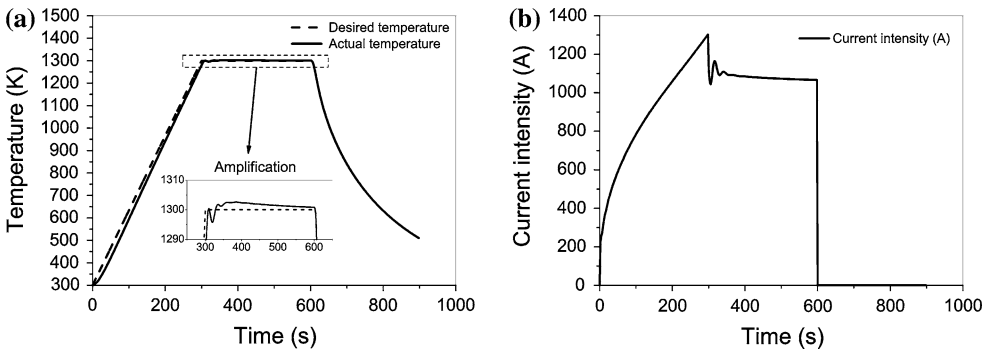

Fig. 5 **a** Temperature evolution of control point (point A in Fig. 4), and **b** applied current intensity, for the alumina sample case with PID controller

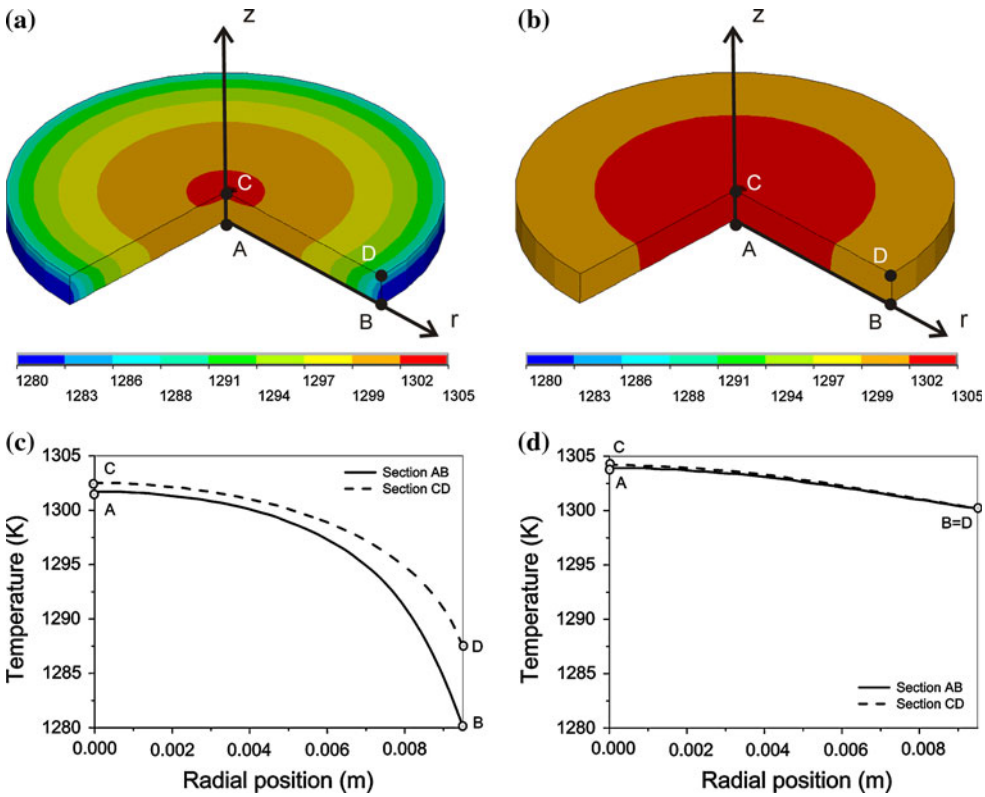

Fig. 6 Temperature distribution inside the **a** alumina and **b** Cu samples. Temperature distribution along the lines AB and CD of the sample section for **c** alumina and **d** Cu samples. All at time $t = 350$ s (Same temperature scale for all graphs)

densification mechanisms, the differences in temperature observed in the alumina sample could affect the homogeneity of the microstructure, while no problems are expected in the case of copper. These results refer to the situation at a time in the simulation (t = 350 s) corresponding to the end of the temperature increase, and in general their features agree quite well with what has been already reported by other authors in the case of steady-state solutions [5–11]. With our approach, however, it is possible to follow the evolution of the temperature profiles during a temperature-controlled experiment where a linear temperature increase is imposed on the sample. In Fig. 7, the time evolution of the temperature at the four points of the studied section (points A, B, C and D) is shown. Note that, for clarity, only the range close to the target temperature of 1300 K has been reported. In the alumina sample (Fig. 7a), practically no differences in temperature are observed between the centre points, A and C, during the process. However, significant differences with the other two points (B and D) are encountered. These temperature differences increase from the beginning of the experiments and reach the maximum values at the end of the heating ramp, at time $t = 300$ s, where there is a difference of 34 K (a 2.6%) between points C and B. After stabilisation, during the steady-state period (between 300 and 600 s), the temperature differences remain constant, and at time t = 600 s, when the current is turned off, the temperature differences vanish progressively due to heat losses by conduction and radiation. In the copper sample (Fig. 7b), no differences in temperature in the axial direction and little differences in the radial direction are observed along the entire experiment.

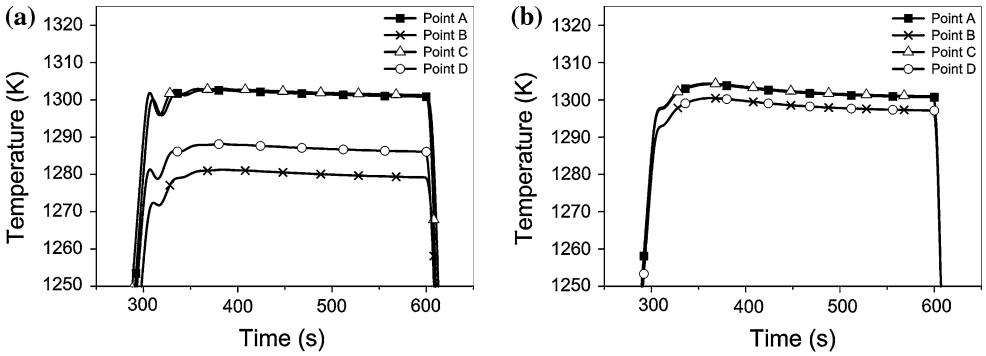

Fig. 7 Evolution of temperature at points A, B, C and D, for **a** alumina and **b** Cu samples. Represented only the interest zone, near 1300 K

Stress distribution

Our analysis of stress distribution under static conditions produced results similar to those presented by Wang et al. [11] and by Antou et al. [10], although in this last paper samples different from ours are considered. In the case of alumina, the radial displacement in the whole assembly increases uniformly with increasing radius. In contrast, for the copper case, the radial displacement in the assembly does not increase uniformly with radial position. The radial displacements are due to the combination of the thermal expansion and the mechanical expansion due to Poisson effect. In an SPS experiment, since high temperatures are reached in the set-up during the process, the thermal contribution in the radial displacement is much larger than the mechanical one. Thus, differences in radial displacement between the alumina and copper cases can be explained by differences in the thermal expansion coefficient of the three materials involved (alumina, copper and graphite) [11]. Since alumina and graphite have similar thermal expansion coefficients, the sample and the die expand together, and no distortion is observed. However, in the case of copper, due to the high thermal expansion coefficient of the metal compared with that of graphite, the sample exhibits a great expansion and pushes the die wall, causing an important deformation in the radial direction.

The stress analysis reported previously by Wang et al. [11] and by Antou et al. [10] is based on the analysis of the stress tensor components. This approach is essential in order to explain the stress field inside the sample, but it could be confusing and difficult to understand, since four components of the stress tensor (σ_z, σ_r, σ_θ and σ_{rz}) are studied simultaneously. A better understanding of the evolution of the stress distribution inside the sample and its influence on the densification process can be obtained by a representative scalar stress value computed from the stress tensor. For this purpose, the hydrostatic stress can be used. The hydrostatic stress or mean stress is defined as $\sigma_h = \frac{1}{3} I_1$, where I_1 is the first stress invariant, which can be calculated by the principal stresses ($I_1 = \sigma_1 + \sigma_2 + \sigma_3$), or by the normal components of the stress tensor ($I_1 = \sigma_z + \sigma_r + \sigma_\theta$). This scalar value is the magnitude of the hydrostatic stress tensor, which is the part of the stress tensor responsible for the change of volume. Thus, this parameter represents quite well the state of the densification process and is included in most of the powder compaction models [18]. In Fig. 8, the hydrostatic stress distribution inside the sample is plotted, at time t = 350 s, for both alumina and copper. In both cases, a non-homogenous distribution of the hydrostatic stress is observed. In the alumina sample, shown in Fig. 8a, the hydrostatic stress has a maximum value in compression of 39 MPa in the centre of the sample (points A and C) and decreases progressively in the radial direction. In Fig. 8c, it can be seen more clearly that the most significant differences are encountered in the radial direction (18 MPa between points A and B, at 46%), while the differences in the axial direction are negligible at the edge of the sample (6 MPa between points B and D, at 22%). In contrast, much higher values of the hydrostatic stress are observed in the copper sample, as shown in Fig. 8b. In this case, the value in the centre of the sample is of 336 MPa in compression, which is 8.6-times higher than that in the alumina sample. Figure 8d shows that the hydrostatic stress distribution is very homogeneous inside the copper sample, except at the edge of the sample, where the maximum difference is observed (138 MPa between points B and D, at 38%). The homogeneity in the stress distribution inside the specimen depends on the difference in expansion experienced between the sample and its surrounding. Thus, larger differences in the thermal expansion coefficient between the sample and the die lead to larger stresses inside the specimen (much larger stresses are observed in the copper sample than in the alumina one). In conclusion, because pressure has an important role in the densification mechanisms, the differences in stresses observed in both cases could affect the homogeneity of the microstructure. In the case of copper, although the densification process could be accelerated due to the higher pressure experienced by the sample, the stress differences inside the sample are critical in the process, and a different microstructure can be expected at the edge of the sample.

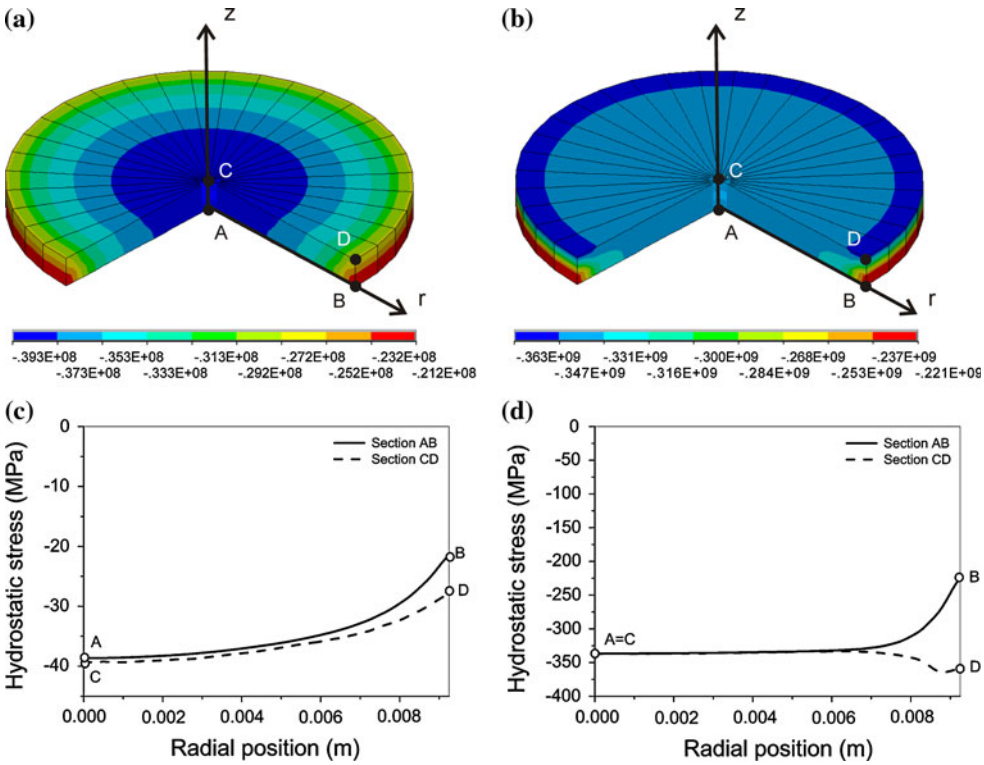

Fig. 8 Hydrostatic stress distribution inside the **a** alumina and **b** Cu samples. Hydrostatic stress distribution along the lines AB and CD of the sample section for the **c** alumina and **d** Cu samples. All at time $t = 350$ s

A more complete understanding of the role of stress distribution in determining sample microstructure can be obtained from the analysis of its time evolution. Figure 9 shows the hydrostatic stress evolution of four points of the studied section (points A, B, C and D). In the alumina sample (Fig. 9a), the four points show an initial value of ~11 MPa (due to the mechanical pressure applied at the beginning of the process) that increases gradually with time until stabilisation at time $t = 300$ s. In the steady-state period, from 300 to 600 s, the centre points A and C experience the same hydrostatic stress of 39 MPa, while a significantly lower stress is observed in the points at the edge of the sample, especially in point B (21 MPa, at 46% lower). At time $t = 600$ s, when the current is turned off, all points experience a sharp increase in compressive stress followed by a rapid decrease. This peak is caused by the differences in thermal conductivities between the sample and the die. At 600 s, the cooling stage begins, where heat is evacuated by conduction towards the external surfaces and by radiation towards the chamber walls. At this time, due to the higher thermal conductivity of graphite compared with alumina, heat is evacuated more efficiently from the graphite and its temperature decrease more rapidly. As a result, graphite suffers a larger contraction than the sample, producing compressive stresses inside the sample. In the copper sample (Fig. 9b), the magnitude of stresses is much larger than in the case of alumina. The values of the stresses increase linearly during the heating ramp and reach maximum values at time $t = 300$ s. During the steady-state period, from 300 to 600 s, very high differences in stresses are observed between the centre and the edge of the sample (a difference of 138 MPa between points D and B, at 38%). In this case, at time $t = 600$ s, when the current is turned off, no peaks in stresses are observed in the copper sample. Due to the high thermal conductivity of the copper, an efficient evacuation of heat is experienced by the sample during the cooling stage, and no differences in contraction between the sample and the die are observed.

From the analysis of the stress time evolution in the sample, an important conclusion can be drawn: in the case of alumina, sharp peaks in stresses are experienced by the sample at the beginning of the cooling stage (Fig. 9a), which could reach values high enough to produce the failure of the sample. For this reason, as practical recommendation, special care must be taken in the cooling stage in the case of non-conducting samples characterised by low thermal conductivities. In order to avoid this problem, controlled cooling stages can be used. In Fig. 10 the results of the hydrostatic stress evolution are shown, corresponding to the time–temperature profile shown at the bottom left of the figure. As observed in Fig. 10, due to the controlled cooling used in the experiment, with a progressive reduction of temperature, the peaks in stresses observed in Fig. 9a have been completely eliminated.

In addition to the stress distribution in the sample, it is also interesting to analyse the stress in the die, plungers and rams, because the graphite strength is the main limitation in determining the maximum load that can be applied in the

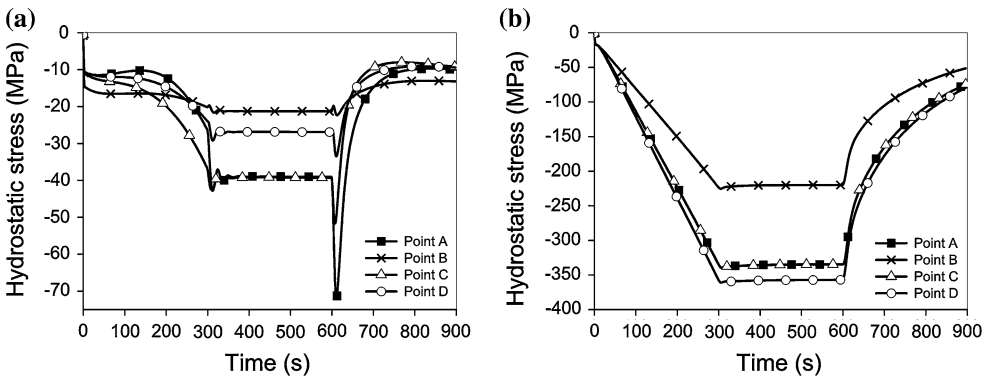

Fig. 9 Evolution of the hydrostatic stress, σ_h, at points A, B, C and D, for **a** alumina and **b** Cu samples

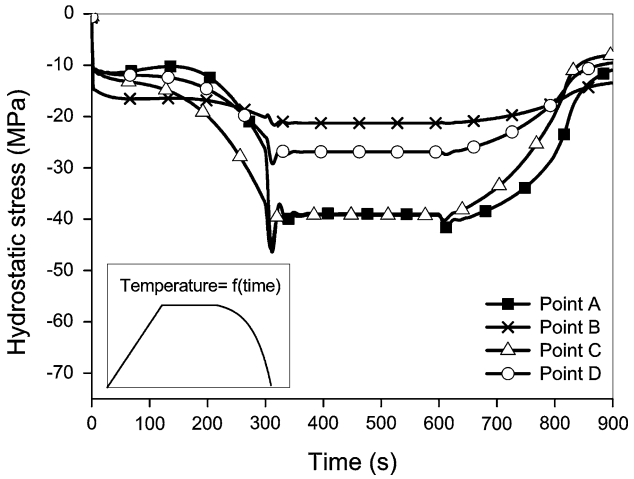

Fig. 10 Evolution of the hydrostatic stress, σ_h, at points A, B, C and D, for alumina sample, in an experiment with a controlled cooling stage

process. For this reason, the distribution of the maximum shear stress, τ_{max}, has been evaluated in the SPS set-up. Figure 11 shows the contour plot of τ_{max} in the SPS set-up, at time $t = 350$ s, when the maximum stresses are reached. Note that the sample has been excluded from the plots. In the alumina case (Fig. 11a), the maximum value of τ_{max} is observed in the contact zone between the spacer and the punch (49 MPa), but this value is not critical for graphite. However, in the case of copper (Fig. 11b), a maximum value of $\tau_{max} = 183$ MPa is reached in the die at the zone in contact with the sample, due to the larger expansion of the sample that pushes the die. This high value of τ_{max} could cause the failure of the graphite die and must be taken into account.

Conclusions

To allow a better understanding of the SPS process, the time evolution of the current density, temperature and stress distribution during the process has been analysed. Comparison between simulations and experiments has demonstrated the accuracy of the proposed finite element model. Making use of a PID control integrated into the model, more realistic experiments have been simulated and discussed, paying particular attention to the time evolution of the process. On the basis of the presented results, the following conclusions can be drawn:

- The current density distribution in the sample and its proximity depends on the electrical conductivity of the sample: no current flows through the alumina sample, while an important fraction of the total current is carried by the copper sample.
- The temperature distribution inside the specimen is governed mainly by its thermal conductivity: the lower

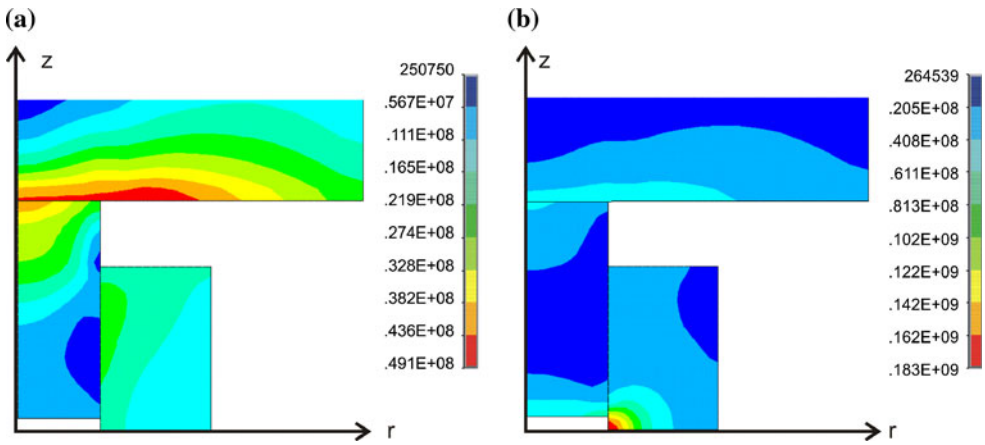

Fig. 11 Maximum shear stress distribution in the set-up, for **a** alumina and **b** Cu samples. All at time $t = 350$ s

thermal conductivity of alumina leads to a non-homogeneous temperature distribution with significant gradients, while the higher thermal conductivity of copper leads to a homogeneous temperature inside the sample.
- Differences in temperature observed in the alumina sample (a maximum difference of 2.6%) could affect the homogeneity of the microstructure, while no problems are expected in the case of copper.
- During the evolution of the process, temperature differences in the samples increase linearly and reach maximum values at the end of the heating ramp. During the steady period, temperatures remain constant, and when the current is turned off, the temperature differences vanish progressively due to heat losses by conduction and radiation.
- For the stress analysis, the scalar hydrostatic stress σ_h resulted to offer a better representation of the actual situation as it is more directly linked to the densification process.
- The magnitude of stresses in the sample depends on the difference in thermal expansion between the sample and its surrounding: larger differences in the thermal expansion between the sample and the die produce larger stresses inside the sample.
- For both kinds of samples considered (copper and alumina), non-homogenous stress distributions have been observed. In alumina, the most significant difference in stresses is encountered in the radial direction (46% difference). In copper, the stress distribution is very homogeneous, except at the edge of the sample, where an important stress gradient (38% difference) in the axial direction is observed.
- Since stress gradients in the samples are much greater than temperature gradients, it is suggested that stress distribution plays a significant role in controlling the microstructure in SPS samples.
- The dynamic evolution of the stress distribution during the SPS process is similar for both kinds of samples and shows a gradual increment during the heating ramp, a steady-state period and, finally, a progressive decrease during the cooling period.
- In the case of alumina, a peak in the stress values is observed in the sample at the beginning of the cooling stage (time t = 600 s). This is caused by differences in contraction between the sample and the die, due to the low thermal conductivity of the alumina.
- These peaks in stresses observed in the alumina samples could reach such high values to produce the failure of the sample. It has been proven that, using a controlled cooling stage, peaks in stresses can be easily eliminated.
- In the case of alumina samples, the stress values observed in the graphite die, plungers and rams never reach a critical value for the applied load, but in the case of copper, large stresses are observed in the die at the contact with the sample, which could eventually cause the failure of the graphite die.

Acknowledgements The authors would like to thank T. Holland at the Department of Chemical Engineering and Materials Science at UC Davis for performing the SPS experiments. The first author would like to acknowledge the mobility grant from the "José Castillejo" program, and the financial support from the FEDER/MEC, Madrid (Project MAT2007-61643).

Appendix

Graphite properties

$$\rho\left(\mathrm{Kg\ m^{-3}}\right) = 1900;\ E\,(\mathrm{Pa}) = 103\times10^{9};\ v = 0.32;\quad \alpha_T = 8\times10^{-6}$$

$$C_p\left(\mathrm{J\ kg^{-1}\ K^{-1}}\right) = -398.1737 + 4.5879T - 3.5288\times10^{-3}T^2 + 1.2869\times10^{-6}T^3 - 1.8215\times10^{-10}T^4$$

$$k\left(\mathrm{W\ m^{-1}\ K^{-1}}\right) = 90 - 9.5411\times10^{-2}T + 8.1687\times10^{-5}T^2 - 3.2096\times10^{-8}T^3 + 4.7799\times10^{-12}T^4$$

$$\rho_e\left(\mathrm{W\ m^{-1}\ K^{-1}}\right) = \sigma^{-1} = 2.3982\times10^{-5} - 2.5707\times10^{-8}T + 2.1464\times10^{-11}T^2 - 8.2881\times10^{-15}T^3 + 1.2197\times10^{-18}T^4$$

Stainless steel (AISI 304) properties

$$\rho\left(\mathrm{Kg\ m^{-3}}\right) = 7900;\ E\,(\mathrm{Pa}) = 200\times10^{9};\ v = 0.33;\quad \alpha_T = 18\times10^{-6}$$

$$C_p\left(\mathrm{J\ kg^{-1}\ K^{-1}}\right) = 446.5 + 0.162T$$

$$k\left(\mathrm{W\ m^{-1}\ K^{-1}}\right) = 9.988 + 0.01746T$$

$$\rho_e\left(\mathrm{W\ m^{-1}\ K^{-1}}\right) = \sigma^{-1} = 10^{-8}[50.1685 + 0.0838T - 1.7453\times10^{-5}T^2]$$

Alumina properties

$$\rho\left(\mathrm{Kg\ m^{-3}}\right) = 3970;\ E\,(\mathrm{Pa}) = 215\times10^{9};\ v = 0.32;\quad \alpha_T = 8\times10^{-6}$$

$$C_p\left(\mathrm{J\ kg^{-1}\ K^{-1}}\right) = -126.5317 + 8.1918T - 6.1058 \times 10^{-3}\,T^2 + 2.3104 \times 10^{-6}T^3 - 3.4204 \times 10^{-10}T^4$$

$$k\left(\mathrm{W\,m^{-1}\,K^{-1}}\right) = 76.4488 - 0.18978T + 1.9596 \times 10^{-4}\,T^2 - 8.9466 \times 10^{-8}\,T^3 + 1.4909 \times 10^{-11}\,T^4$$

$$\rho_e\left(\mathrm{W\,m^{-1}\,K^{-1}}\right) = \sigma^{-1} = 10^{-8}$$

Copper properties

$$\rho\left(\mathrm{Kg\ m^{-3}}\right) = 8960;\ E(\mathrm{Pa}) = 110 \times 10^9;\ v = 0.33;\quad \alpha_{\mathrm{T}} = 15 \times 10^{-6}$$

$$c_p\left(\mathrm{J\ kg^{-1}\ K^{-1}}\right) = 355.3 + 0.1T$$

$$k\left(\mathrm{W\,m^{-1}\,K^{-1}}\right) = 420.66 - 0.07T$$

$$\rho_{\mathrm{e}}\left(\mathrm{W\ m^{-1}\ K^{-1}}\right) = \sigma^{-1} = 10^{-9}\left[-3.44 + 70.9 \times 10^{-3}\,T - 9.6 \times 10^{-6}\,T^2 + 9.77 \times 10^{-9}\,T^3\right.$$

References

1. Groza JR (1998) In: ASM Handbook, vol 7, Powder metallurgy, pp 583
2. Orrù R, Licheri R, Locci A, Cincotti A, Cao G (2009) Mater Sci Eng R 63:127–287
3. Munir ZA, Anselmi-Tamburini U, Ohyanagi M (2006) J Mater Sci 41:763–777. doi:10.1007/s10853-006-6555-2
4. Anselmi-Tamburini U, Garay JE, Munir ZA (2006) Scr Mater 54:823–828
5. Zavaliangos A, Zhang J, Krammer M, Groza JR (2004) Mater Sci Eng A 379:218–228
6. Vanmeensel K, Laptev A, Hennicke J, Vleugels J, Van der Biest O (2005) Acta Mater 53:4379–4388
7. Anselmi-Tamburini U, Gennari S, Garay JE, Munir ZA (2005) Mater Sci Eng A 394:139–148
8. McWilliams B, Zavaliangos A, Cho KC, Dowding RJ (2006) JOM 58(4):67–71
9. McWilliams B, Zavaliangos A (2008) J Mater Sci 43(14):5031–5503. doi:10.1007/s10853-008-2744-5s
10. Antou G, Mathieu G, Trolliard G, Maitre A (2009) J Mater Res 24(2):404–412
11. Wang X, Casolco SR, Xu G, Garay JE (2007) Acta Mater 55:3611–3622
12. ANSYS 11.0 Coupled-field analysis guide (2007)
13. ANSYS 11.0 Contact technology guide (2007)
14. Åstrom KJ, Hagglund T (1995) PID controllers: theory, design and tuning, 2nd edn. ISA Research Triangle Park, NC
15. Ziegler J, Nichols N (1942) Trans ASME 64:759–768
16. Matsugi K, Kuramoto H, Hatayama T, Yanagisawa O (2004) J Mater Process Technol 146:274–281
17. Tomino H, Watanabe H, Kondo Y (1997) J Jpn Soc Powder Metall 44:974–979
18. Khoei A (2005) Computational plasticity in powder forming processes, Elsevier Sci, Oxford